J Appl Electrochem (2012) 42:263–269
DOI 10.1007/s10800-012-0393-5

ORIGINAL PAPER

Enhanced electrochemical performance of FeS_2 synthesized by hydrothermal method for lithium ion batteries

D. Zhang · X. L. Wang · Y. J. Mai · X. H. Xia · C. D. Gu · J. P. Tu

Received: 28 November 2011 / Accepted: 13 February 2012 / Published online: 24 February 2012

Abstract Iron disulfide (FeS_2) powders were successfully synthesized by hydrothermal method. Cetyltrimethylammonium bromide (CTAB) had a great influence on the morphology, particle size, and electrochemical performance of the FeS_2 powders. The as-synthesized FeS_2 particles with CTAB had diameters of 2–4 μm and showed a sphere-like structure with sawtooth, while the counterpart prepared without CTAB exhibited irregular morphology with diameters in the range of 0.1–0.4 μm. As anode materials for Li-ion batteries, their electrochemical performances were investigated by galvanostatic charge–discharge test and electrochemical impedance spectrum. The FeS_2 powder synthesized with CTAB can sustain 459 and 413 mAh g^{-1} at 89 and 445 mA g^{-1} after 35 cycles, respectively, much higher than those prepared without CTAB (411 and 316 mAh g^{-1}). The enhanced rate capability and cycling stability were attributed to the less-hindered surface layer and better electrical contact from the sawtooth-like surface and micro-sized sphere morphology, which led to enhanced process kinetics.

Keywords Iron disulfide · Marcasite · Rate capability · Cycling performance

D. Zhang · X. L. Wang (✉) · Y. J. Mai · X. H. Xia · C. D. Gu · J. P. Tu (✉)
State Key Laboratory of Silicon Materials and Department of Materials Science and Engineering, Zhejiang University, Hangzhou 310027, China
e-mail: wangxl@zju.edu.cn

J. P. Tu
e-mail: tujp@zju.edu.cn

1 Introduction

Iron disulfide (FeS_2) is an attractive anode material for lithium ion batteries because of its interesting characteristics such as high theoretic capacity (890 mAh g^{-1}), low environmental impact and affordable cost [1–16]. However, the capacities of FeS_2 electrodes often reduce very quickly during charge–discharge cycling, especially at high current densities. For instance, Montoro et al. [17] found that the gelatin-pyrite composite electrode could only sustain 279 mAh g^{-1} after 15 cycles in the voltage range of 1.1–3.2 V (vs. Li/Li^+) at 0.4 mA cm^{-2}. Huang et al. [3] prepared FeS_2 film which delivered discharge specific capacity of 442 mAh g^{-1} for the second cycle at 50 μA cm^{-2}. Choi et al. [18] reported that nickel-precipitated pyrite exhibited initial discharge capacity of 600 mAh g^{-1} at 89 mA g^{-1} between 0.8 and 2.4 V (vs. Li/Li^+).

The morphology is the key point to determine the capacity and cyclability of FeS_2 [19–26]. For example, microsized particulate exhibits better cycling performance than the nanosized one [27, 28]. Therefore, it is very urgent to prepare FeS_2 with appropriate morphology to improve its electrochemical performances. As is known to all, hydrothermal method is a commonly used approach to control the morphology of as-prepared materials. Cetyltrimethylammonium bromide (CTAB) is usually used as surfactant to modify the morphology of particles [29, 30]. For example, copper oxide spheres with needle-like morphology obtained in the presence of CTAB shows higher specific capacity than bird nest-like morphology obtained without CTAB [19]. However, as far as we know, there are little literatures on electrochemical performances of FeS_2 synthesized by hydrothermal method.

In the present work, irregular and sphere-like FeS_2 particles (pyrite and marcasite) are synthesized by hydrothermal method. The influence of CTAB surfactant on the

morphology of FeS_2 is discussed, and the improved electrochemical performances including both the capacity and cycling stability are investigated.

2 Experimental

FeS_2 powder was synthesized by a surfactant assisted hydrothermal method. In a typical synthesis, 13.9 g of $FeSO_4{\cdot}7H_2O$ and 12.4 g of $Na_2S_2O_3$ were dissolved in 25 mL of de-ionized water under magnetic stirring. 0.8 g of S powder and 0.2 g of CTAB were added to the resulting solution under vigorous magnetic stirring at room temperature for 1 h. Then this mixture was sealed in a Teflon-lined stainless steel autoclave (50% filled), maintained at 200 °C for 24 h, and cooled to room temperature naturally. Afterward, the black solid product was collected by centrifugation, washed with absolute alcohol, CS_2 and de-ionized water several times, and finally dried in vacuum at 100 °C for 10 h. The sample prepared without CTAB is also obtained in the same way for comparison.

The as-synthesized powders were characterized by X-ray diffraction (XRD, D/max 2550-PC), field emission scanning electron microscopy (FESEM, FEI SIRION) and transmission electron microscopy (TEM, TECNAI F20). The X-ray powder diffraction measurements were performed on a Rigaku D/Max-2550-pc powder diffractometer, using Cu-Kα (λ for Kα = 1.54059 Å) radiation at 40 kV and 250 mA. The scans were run from 10 to 100° 2θ, with an increasing step size of 0.02° and counting time duration of 3 s for each step. Data were processed using the MDI-Jade version 7.0 software. The specific surface area of the samples were calculated following the multipoint Brunauer–Emmett–Teller (BET) procedure from the N_2 adsorption–desorption isotherms collected at liquid nitrogen temperature using an AUTOSORB-1-C gas sorption analyzer.

Electrochemical performances of FeS_2 were investigated in CR2025 coin-type cell. The working electrode consisted of as-synthesized material (60 wt%), acetylene black (25 wt%), and polyvinylidene fluoride binder (15 wt%) on aluminum foil. A metallic lithium foil served as the counter electrode. The cells were assembled in an argon-filled glove box using 1 M $LiPF_6$ in ethylene carbonate (EC)–dimethyl carbonate (DMC) (1:1 in volume) as the electrolyte and a polypropylene micro-porous film (Cellgard 2300) as the separator. The charge–discharge tests were conducted on LAND battery program–control test system (Wuhan, China) using potentials between 1.2 and 2.6 V and applying from 89 to 445 mA g^{-1} at room temperature. Electrochemical impedance spectrum (EIS) was performed on CHI 660C electrochemical workstation. The assembled cells were used for EIS tests, where lithium foils acted as both the counter and reference electrodes. EIS measurements were performed over a frequency range from 100 kHz to 10 mHz under AC stimulus with 5 mV of amplitude and no applied voltage bias. The impedance data were fitted using the ZsimpWin computer program.

3 Results and discussion

Figure 1 shows XRD patterns of FeS_2 powders synthesized without and with CTAB. As shown in the figure, the two samples exhibit similar XRD pattern. Some diffraction peaks correspond well with the cubic pyrite FeS_2 (PDF card No. 42-1340). Other diffraction peaks can be indexed to the marcasite FeS_2 (PDF card No. 37-0475). The diffraction peak which is indexed to (200) plane of pyrite for FeS_2 powder synthesized with CTAB is stronger than the other one, and the intensity of the diffraction peak indexed to (111) plane is the same for the two samples, indicating the preferential growth along the (200) direction. The structures of pyrite and marcasite contain similar features along certain crystallographic directions [31]. The thermodynamic and structural similarities of the two iron disulfide polymorphs make it difficult to prepare single phase. The contents of marcasite are calculated to be 43.3 and 42.1 wt% for the FeS_2 powders synthesized without and with CTAB by Rietveld refinement, respectively. The content of marcasite is almost the same for the two samples. Thus, it is reasonable to compare the electrochemical properties of the two samples without considering the difference in the compositions between the two powders.

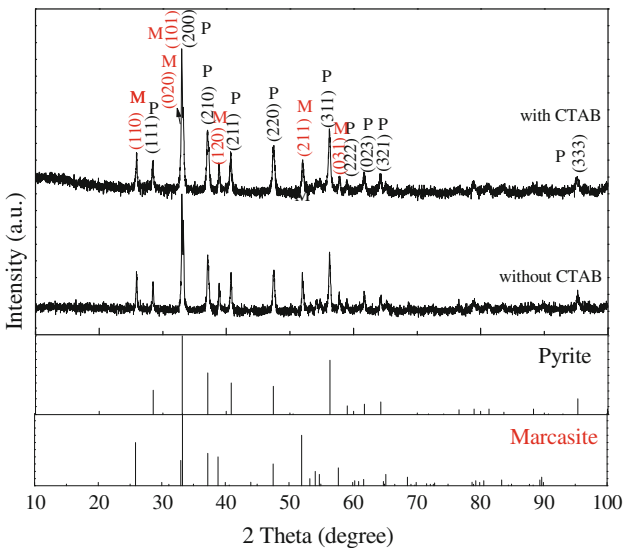

Fig. 1 XRD patterns of FeS_2 powders synthesized without and with CTAB

Morphologies of FeS_2 particles synthesized with and without CTAB are shown in Fig. 2. Irregular particles with sizes of 0.1–0.4 μm can be observed for the FeS_2 compound synthesized without CTAB in Fig. 2a. Most particles show sharp edges and corners. The similar morphology is also observed in other works [6, 8]. FeS_2 particles obtained in the existence of CTAB show sphere-like appearance with submicro-sawtooth on their surface (Fig. 2b). Each sawtooth is about 0.1–0.3 μm in width. Diameters of spheres are about 2–4 μm which are much larger than those of the FeS_2 particles synthesized without CTAB. In addition, the BET surface areas are 3.5 and 6.0 $m^2\ g^{-1}$ for FeS_2 particles with and without CTAB, respectively. The BET results are well consistent with the SEM images.

Obviously, the varying morphologies of FeS_2 particles are associated with the surfactant effect of CTAB. The growth process of FeS_2 synthesized without CTAB is presented in Ref. [6]. The formation reaction for FeS_2 can be summarized as follows:

$$Na_2S_2O_3 + S + FeSO_4 + H_2O \rightarrow Na_2SO_4 + FeS_2 + H_2SO_4 \quad (1)$$

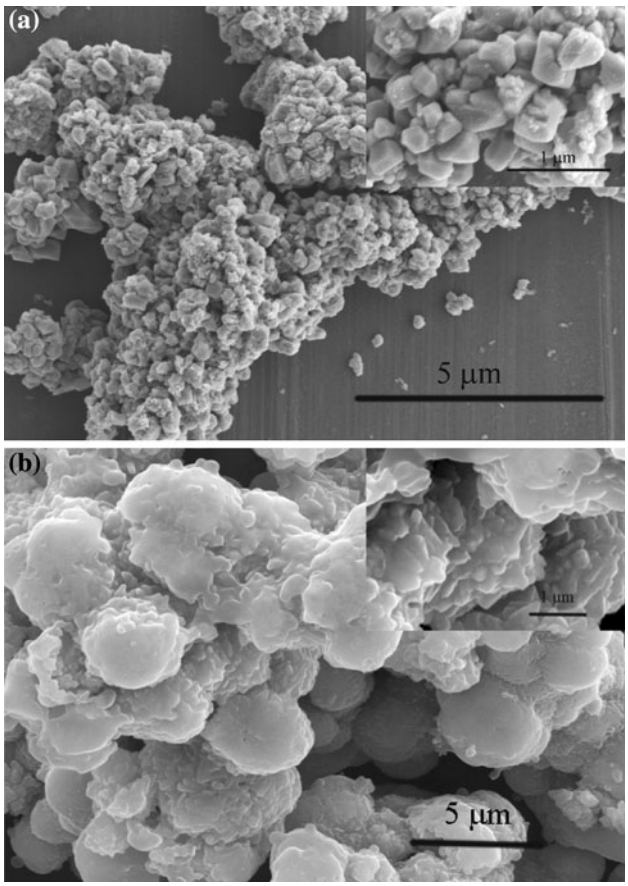

Fig. 2 SEM images of FeS_2 particles synthesized **a** without and **b** with CTAB

Although crystal growth mechanisms of pyrite and marcasite compounds in solution have been investigated in some early literatures, they still remain unclear [6, 8]. It is considered that the geometric shape of a pyrite crystal is determined by the ratio (R) of the growth rate along the [100] direction to that along the [111] direction [12, 32]. In this work, the R value of the pyrite FeS_2 powder with CTAB is larger than that of the other one according to the XRD pattern. It has become apparent that a certain amount of CTAB may favor the pyrite crystal growth along the [100] direction and make it exceed that of [111] direction. Therefore, {111} faces expansion at the expense of {100} faces. The surface energy of pyrite {111} is higher than that of {100} faces, thus crystals form skeleton spheres via self-organization to minimize the total surface energy [33]. Then the sphere-like morphology with sawtooth-like surface is formed. However, the crystal growth mechanism in solution is intricate, the actual crystallization processes for FeS_2 crystals remain unclear and much work still is needed for further study.

Figure 3 shows the discharge–charge profiles of a few representative cycles, namely cycle 1, 5, 10, 20, and 30 between 1.2 and 2.6 V at 89 mA g^{-1}. Both the first discharge curves show an abrupt drop in voltage, followed with a long plateau between 1.4 and 1.45 V. The first discharge plateau is associated with the formation of Fe, Li_2S, and Li-rich phases depending on the quantity of lithium transfer per FeS_2 [2, 34, 35]. The subsequent discharge curves differ from the first one, indicating a change in the mechanism of pyrite reduction. The discharge curves show two plateaus at about 1.5 and 2.0 V. The charge curves show two plateaus at about 1.8 and 2.45 V. However, there are still some differences in discharge–charge curves of the two electrodes. The FeS_2 powder synthesized without CTAB exhibits a little longer plateau, smaller polarization, and higher initial capacity (832 mAh g^{-1}) than the one synthesized with CTAB (818 mAh g^{-1}) at 89 mA g^{-1}. The high initial capacity of FeS_2 synthesized without CTAB can be attributed to the large specific area between the active material and electrolyte, offering a great deal of sites to accommodate Li^+ due to the small particles. However, the polarization increases obviously for the FeS_2 powder synthesized without CTAB during the following cycling. On the other hand, for the FeS_2 powder synthesized with CTAB, the polarization first reduces and then increases little during the following cycling. As is well known, the delay in the transfer of electrons and lithium ions on the active material/electrolyte interface can result in the polarization in lithium ion batteries [36]. It is indicated that electrons and lithium ions can transfer more easily on the active material/electrolyte interface of the FeS_2 synthesized with CTAB.

Nyquist plots of FeS_2 electrodes at a discharge state after the 1st and the 10th cycles in the frequency range of

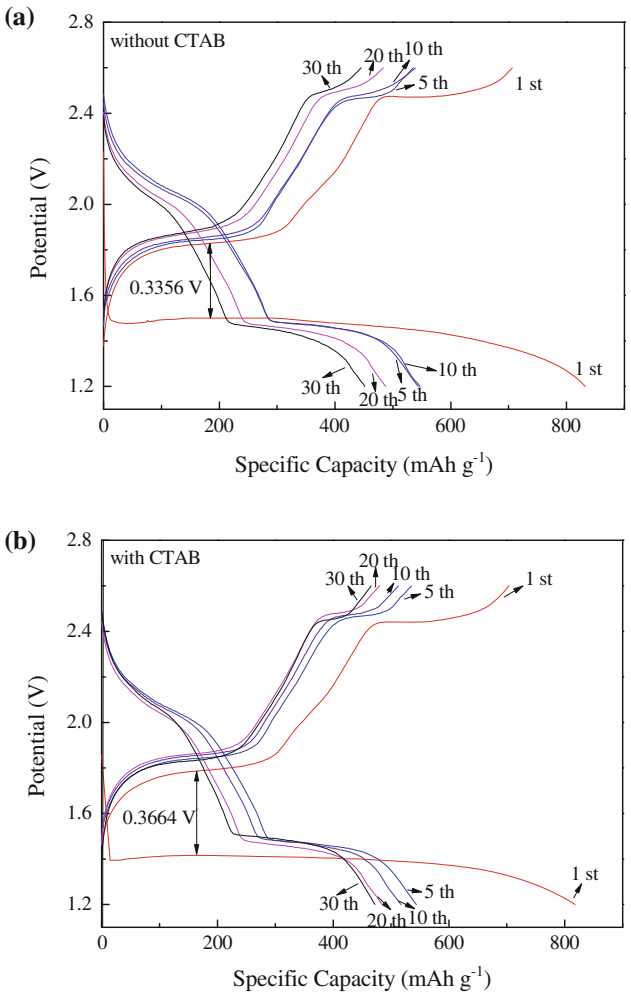

Fig. 3 Discharge–charge curves of FeS_2 electrodes **a** without CTAB and **b** with CTAB between 1.2 and 2.6 V at 89 mA g^{-1}

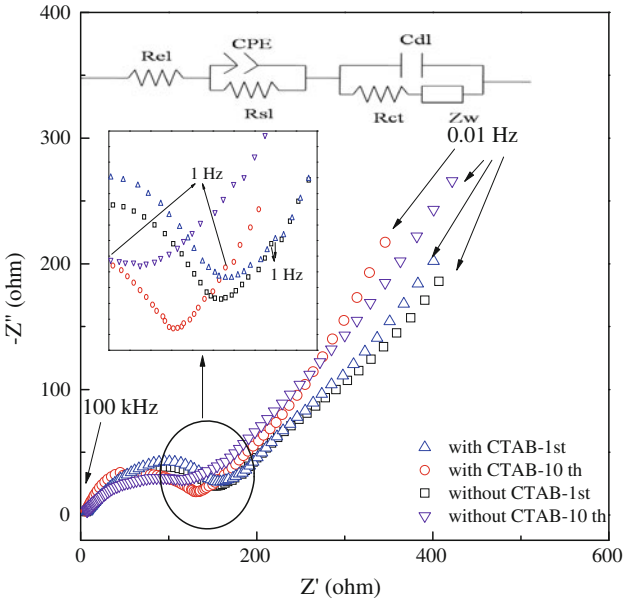

Fig. 4 Nyquist plots of FeS_2 electrodes at a discharge state after the 1st and the 10th cycles in the frequency range of 100 kHz to 0.1 Hz

100 kHz to 0.1 Hz are shown in Fig. 4. Equivalent circuit model for the FeS_2 electrodes is also provided. It consists of the solution resistance (R_{el}), Li^+ migration resistance (R_{sl}), a constant phase element (CPE) instead of pure capacitance (due to the observation of a depressed semicircle), the related charge-transfer resistance (R_{ct}), double-layer capacitance (C_{dl}), and the diffusion-controlled Warburg impedance (Z_w) [37–39]. The values of R_{sl} are 163.9 and 189.7 Ω after the first cycle for the FeS_2 electrodes synthesized without and with CTAB, respectively. After 10 cycles, it is also observed that R_{sl} of the FeS_2 electrode synthesized with CTAB is 111.1 Ω, which is much lower than that (156.5 Ω) of the other one. It indicates that the electrons and Li ions can transfer more quickly on the surface layer of the FeS_2 synthesized with CTAB. The phenomenon that the surface resistance decreases after first cycle is also reported in the previous work [40].

The cycling performances for the FeS_2 electrodes at 89 and 445 mA g^{-1} are displayed in Fig. 5. After 35 cycles, the FeS_2 electrode synthesized with CTAB can sustain 459 and 413 mAh g^{-1} at 89 and 445 mA g^{-1}, which are higher than the one synthesized without CTAB. Such a stable behavior has, to our knowledge, been rarely observed, this being a demonstration of the unique features of our electrode material. As seen in the figure, the FeS_2 electrode synthesized without CTAB delivers high discharge capacities during the early 10 cycles. The high capacity can be ascribed to the small particles which have short diffusion length of Li^+ and large specific surface area between the active material and electrolyte. However, after about 10 cycles, the capacity decreases to a value, which is lower than that of the FeS_2 synthesized with CTAB. The fast capacity fade can be mainly associated with the hindered surface layer and poor electrical contact. The large surface area of FeS_2 synthesized without CTAB forms more SEI layer, and thus results in the irreversible capacity during cycling [20, 41, 42]. In addition, poor electronic conductivity of SEI layer causes serious electrical isolation between the active material and electrolyte, leading to a fast fading of electrode [35, 43]. Therefore, the FeS_2 compound synthesized with CTAB exhibits better cycling performance than the one synthesized without CTAB. Similarly, the results that the microsized particulate exhibits better cycling performance than the nanosized particulate have also been reported in previous works [29, 30].

The coulombic efficiency of the two samples at 445 mA g^{-1} is compared in Fig. 5c. As shown in the figure, the FeS_2 powder synthesized with CTAB exhibits a relatively high initial coulombic efficiency and remains

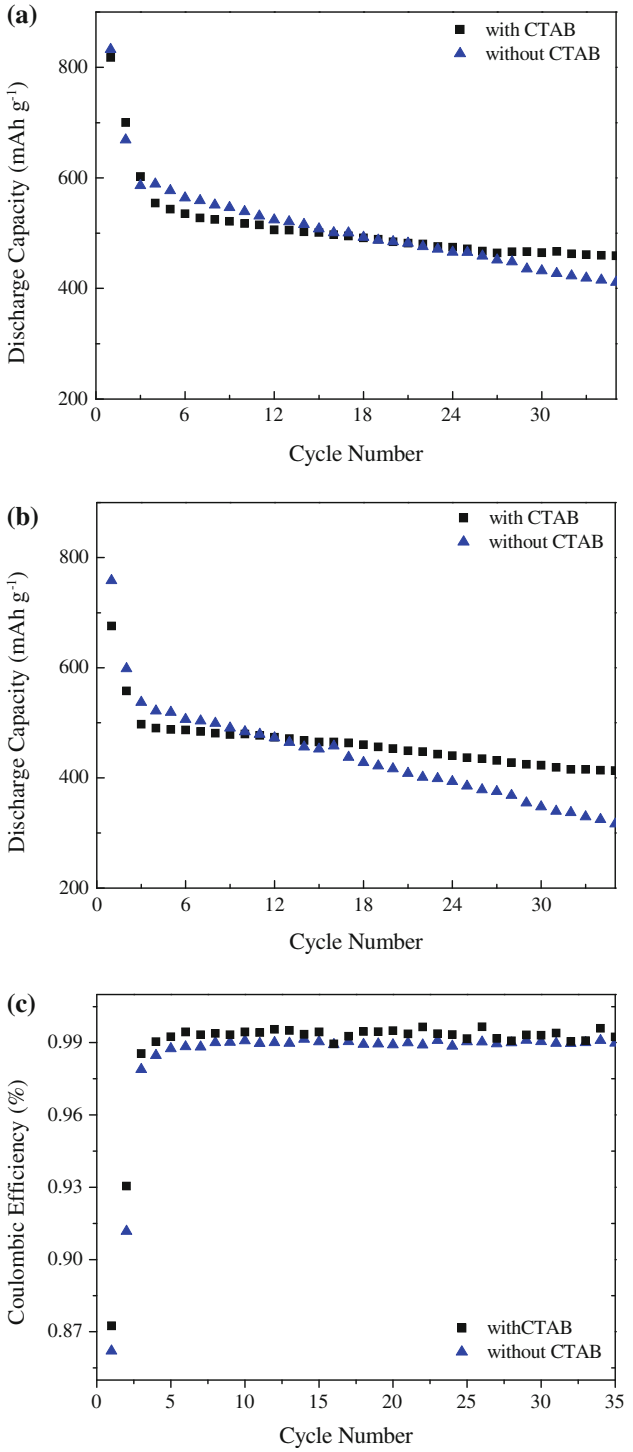

Fig. 5 Cycling performance of FeS_2 electrodes at **a** 89 mA g^{-1}, **b** 445 mA g^{-1} and **c** coulombic efficiency at 445 mA g^{-1} between 1.2 and 2.6 V for 35 cycles

above 99.0% for 35 cycles. However, the electrode without CTAB shows a relatively low coulombic efficiency. The formation and incomplete decomposition of SEI is always the main reason for the low coulombic efficiency for the initial cycle [22, 26]. Smaller active contact area determines the less SEI formation, and thus leads to the higher coulombic efficiency of FeS_2 powder synthesized with CTAB.

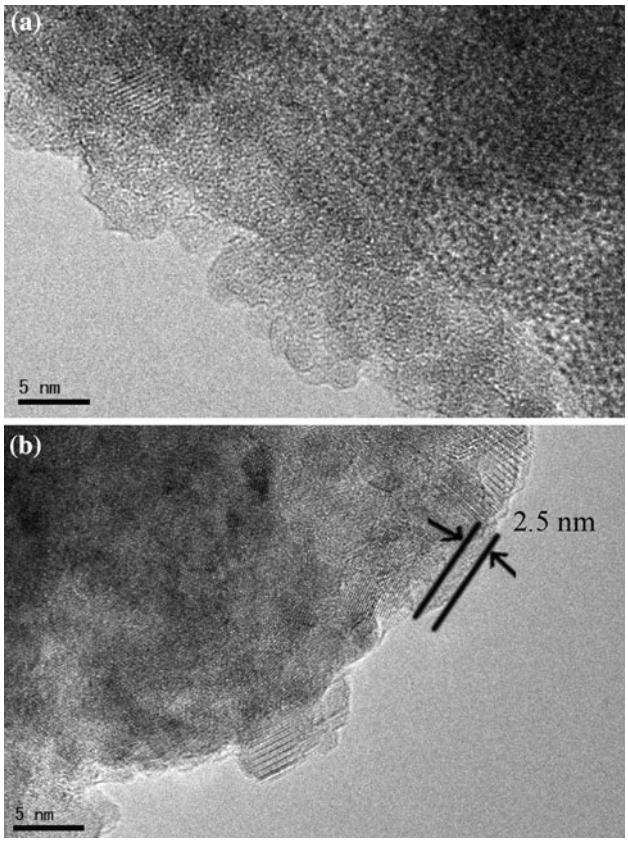

Fig. 6 HRTEM micrographs of FeS_2 electrodes **a** without and **b** with CTAB after 30 cycles in discharge state

HRTEM micrographs would provide more exact and straightforward investigation of the electrochemical process. Figure 6 shows the HRTEM micrographs of the FeS_2 electrodes after 30 cycles in discharge state. The FeS_2 electrode synthesized without CTAB is covered by SEI layer with thickness of 3–8 nm (Fig. 6a), which makes the electron transport more difficult and increases the surface resistance. However, a thinner surface layer with thickness of 1–3 nm is observed around the particles for the FeS_2 electrode synthesized with CTAB (Fig. 6b). It is confirmed that the FeS_2 electrode synthesized with CTAB generates less area of SEI layer on the surface, showing good agreement with the results of Refs. [44, 45].

Considering that the rate capability is also very important for practical applications, we also test the rate capability for FeS_2 electrodes (Fig. 7). The FeS_2 electrode synthesized with CTAB has initial discharge capacities of 731, 456, and 390 mAh g^{-1} at 89, 445, and 890 mA g^{-1}, while the one synthesized without CTAB has an initial discharge capacities of 762, 369, and 284 mAh g^{-1} at 89,

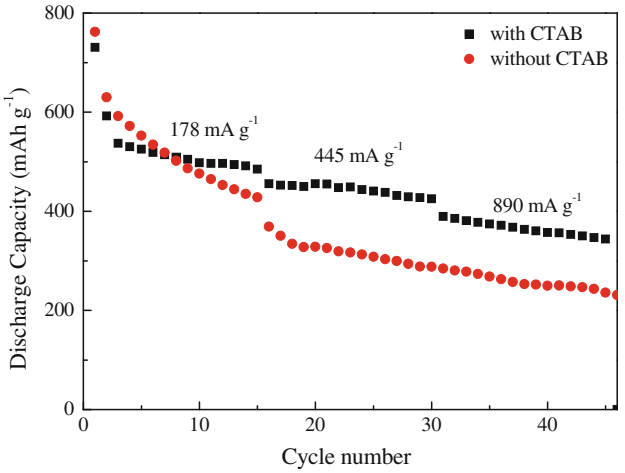

Fig. 7 Rate capability of FeS_2 electrodes between 1.2 and 2.6 V for 45 cycles

445, and 890 mA g^{-1}, respectively. After 45 cycles, the FeS_2 electrode synthesized with CTAB can sustain 344 mAh g^{-1}, which is higher than the other one. The good rate capability is attributed to the less-hindered surface layer and better electrical contact between the active material and electrolyte, leading to enhanced electrode process kinetics.

4 Conclusions

FeS_2 powders were successfully synthesized by hydrothermal method. FeS_2 particles obtained without CTAB show irregular morphology with sharp edges and corners in the range of 0.1–0.4 μm. Under the influence of the surfactant CTAB, FeS_2 particles show sphere-like appearance with submicro-sawtooth on their surface. The FeS_2 powder obtained in the presence of CTAB exhibits a remarkable improved cycling performance, delivering 459 and 413 mAh g^{-1} at 89 and 445 mA g^{-1} after 35 cycles, respectively. Moreover, the rate capability is also greatly improved compared to the one synthesized without CTAB. The improved rate capability and cycling stability can be attributed to the less-hindered surface layer and better electrical contact from the sawtooth-like surface and microsized spheres morphology. The FeS_2 powder synthesized with CTAB is one of the most promising anode materials as candidates for high-energy lithium ion batteries.

References

1. Strauss E, Ardel G, Livshits V, Burstein L, Golodnitsky D, Peled E (2000) J Power Sources 206:88
2. Peled E, Golodnitsky D, Strauss E, Lang J, Lavi Y (1998) Electrochim Acta 1593:43
3. Huang SY, Liu XY, Li QY, Chen J (2009) J Alloy Compd L9:472
4. Ennaoui A, Fiechter S, Goslowsky H, Tributsch H (1985) J Electrochem Soc 1579:132
5. Wu LM, Seo DK (2004) J Am Chem Soc 4676:126
6. Wu R, Zheng YF, Zhang XG, Sun YF, Xu JB, Jian JK (2004) J Cryst Growth 523:266
7. Chen XY, Wang ZH, Wang X, Wan JX, Liu JW, Qian YT (2005) Inorg Chem 951:44
8. Feng X, He XM, Pu WH, Jiang CY, Wan CR (2007) Ionics 375:13
9. Chen XH, Fan R (2001) Chem Mater 802:13
10. Gao P, Xie Y, Ye LN, Chen Y, Guo QX (2006) Cryst Growth Des 583:6
11. Kar S, Chaudhuri S (2004) Chem Phys Lett 22:398
12. Wang DW, Wang QH, Wang TM (2009) CrystEngComm 755:12
13. Wang DW, Wu MH, Wang QH, Wang TM, Chen JA (2011) Ionics 163:17
14. Qian XF, Yin J, Yang YF, Lu QH, Zhu ZK, Lu J (2001) J Appl Polym Sci 2744:82
15. Ahn IS, Kim DW, Kang DK, Park DK (2008) Met Mater Int 14:65
16. Disale SD, Garje SS (2010) Adv Sci Lett 80:3
17. Montoro LA, Rosolen JM (2003) Solid State Ionics 233:159
18. Choi YJ, Kim NW, Kim KW, Cho KK, Cho GB, Ahn HJ, Ahn JH, Ryu KS, Gu HB (2009) J Alloy Compd 462:485
19. Xiang JY, Tu JP, Zhang L, Zhou Y, Wang XL, Shi SJ (2010) Electrochim Acta 1820:55
20. Chou S-L, Lu L, Wang J-Z, Rahman MM, Zhong C, Liu H-K (2011) J Appl Electrochem 1261:41
21. Huang XH, Tu JP, Zeng ZY, Xiang JY, Zhao XB (2008) J Electrochem Soc A438:155
22. Xiang JY, Tu JP, Zhang L, Zhou Y, Wang XL, Shi SJ (2011) J Power Sources 313:195
23. Xu MW, Wang F, Zhao MS, Yang S, Song XP (2011) Electrochim Acta 4876:56
24. Duan JY, Wei BW, Yang RJ, Pan JZ (2010) Funct Mater. Lett 193:3
25. Zhong C, Wang J-Z, Chou S-L, Konstantinov K, Rahman M, Liu H-K (2010) J Appl Electrochem 1415:40
26. Xiang JY, Wang XL, Xia XH, Zhang L, Zhou Y, Shi SJ, Tu JP (2010) Electrochim Acta 4921:56
27. Grugeon S, Laruelle S, Herrera-Urbina R, Dupont L, Poizot P, Tarascon JM (2001) J Electrochem Soc A 285:148
28. Shaju KM, Jiao F, Debart A, Bruce PG (2007) Phys Chem Chem Phys 1837:9
29. Wen ZH, Wang Q, Zhang Q, Li JH (2007) Adv Funct Mater 2772:17
30. Meligrana G, Gerbaldi C, Tuel A, Bodoardo S, Penazzi N (2006) J Power Sources 516:160
31. Spagnoli D, Refson K, Wright K, Gale JD (2010) Phys Rev B 9:81
32. Wang DW, Wang QH, Wang TM (2011) CrystEngComm 3797:12
33. Barnard AS, Russo SP (2007) J Phys Chem C 11742:111
34. Shao-Horn Y, Horn QC (2001) Electrochim Acta 2613:46
35. Golodnitsky D, Peled E (1999) Electrochim Acta 335:45
36. Aurbach D, Markovsky B, Weissman I, Levi E, Ein-Eli Y (1999) Electrochim Acta 67:45
37. Reddy MV, Yu T, Sow CH, Shen ZX, Lim CT, Rao GVS, Chowdari BVR (2007) Adv Funct Mater 2792:17
38. Suresh P, Shukla AK, Munichandraiah N (2002) J Appl Electrochem 267:32
39. Xiang JY, Tu JP, Zhang L, Wang XL, Zhou Y, Qiao YQ, Lu Y (2010) J Power Sources 8331:195

40. Ruffo R, Hong SS, Chan CK, Huggins RA, Cui Y (2009) J Phys Chem C 11390:113
41. Cheng XQ, Shi PF (2005) J Alloy Compd 241:391
42. Jo M, Hong YS, Choo J, Cho J (2009) J Electrochem Soc A 430:156
43. Xiang JY, Tu JP, Qiao YQ, Wang XL, Zhong J, Zhang D, Gu CD (2011) J Phys Chem C 2505:115
44. Zheng T, Gozdz AS, Amatucci GG (1999) J Electrochem Soc 4014:146
45. Winter M, Novak P, Monnier A (1998) J Electrochem Soc 428:145